# High-speed terahertz reflection three-dimensional imaging using beam steering

**Dae-Su Yee,[1,*] Kyong Hwan Jin,[2] Ji Sang Yahng,[1] Ho-Soon Yang,[3] Chi Yup Kim,[1] and Jong Chul Ye[2]**

[1]*Center for Safety Measurement, Korea Research Institute of Standards and Science, 267 Gajeong-ro, Yuseong-gu, Daejeon 305-340, South Korea*

[2]*Department of Bio and Brain Engineering, Korea Advanced Institute of Science and Technology, 291 Daehak-ro, Yuseong-gu, Daejeon 305-701, South Korea*

[3]*Center for Space Optics, Korea Research Institute of Standards and Science, 267 Gajeong-ro, Yuseong-gu, Daejeon 305-340, South Korea*

[*]*dsyee@kriss.re.kr*

**Abstract:** High-speed terahertz (THz) reflection three-dimensional (3D) imaging is demonstrated using electronically-controlled optical sampling (ECOPS) and beam steering. ECOPS measurement is used for scanning an axial range of 7.8 mm in free space at 1 kHz scan rate while a transverse range of 100 × 100 $mm^2$ is scanned using beam steering instead of moving an imaging target. Telecentric f-θ lenses with axial and non-axial symmetry have been developed for beam steering. It is experimentally demonstrated that the non-axially symmetric lens has better characteristics than the axially symmetric lens. The total scan time depends on the number of points in a transverse range. For example, it takes 40 s for 200 × 200 points and 10 s for 100 × 100 points. To demonstrate the application of the imaging technique to nondestructive testing, THz 3D tomographic images of a glass fiber reinforced polymer sample with artificial internal defects have been acquired using the lenses for comparison.



**OCIS codes:** (110.6795) Terahertz imaging; (110.6880) Three-dimensional image acquisition; (110.6960) Tomography; (120.4290) Nondestructive testing.

## References and links

1. Y. Morita, A. Dobroiu, K. Kawase, and C. Otani, "Terahertz technique for detection of microleaks in the seal of flexible plastic packages," Opt. Eng. **44**(1), 019001 (2005).
2. H. Zhong, J. Xu, X. Xie, T. Yuan, R. Reightler, E. Madaras, and X.-C. Zhang, "Nondestructive defect identification with terahertz time-of-flight tomography," IEEE Sens. J. **5**(2), 203–208 (2005).
3. C. Stoik, M. Bohn, and J. Blackshire, "Nondestructive evaluation of aircraft composites using reflective terahertz time domain spectroscopy," NDT Int. **43**(2), 106–115 (2010).
4. B. Ferguson, S. Wang, D. Gray, D. Abbot, and X.-C. Zhang, "T-ray computed tomography," Opt. Lett. **27**(15), 1312–1314 (2002).
5. S. P. Mickan and X.-C. Zhang, "T-ray sensing and imaging," Int. J. Hi. Spe. Ele. Syst. **13**(02), 601–676 (2003).
6. S. Wang, and X.-C. Zhang, "Pulsed terahertz tomography," J. Phys. D Appl. Phys. **37**(4), R1–R36 (2004).
7. W. Withayachumnankul, G. M. Png, X. Yin, S. Atakaramians, I. Jones, H. Lin, B. Ung, J. Balakrishnan, B. W.-H. Ng, B. Ferguson, S. P. Mickan, B. M. Fischer, and D. Abbott, "T-ray sensing and imaging," Proc. IEEE **95**(8), 1528–1558 (2007).
8. N. Sunaguchi, Y. Sasaki, N. Maikusa, M. Kawai, T. Yuasa, and C. Otani, "Depth-resolving THz imaging with tomosynthesis," Opt. Express **17**(12), 9558–9570 (2009).
9. E. Abraham, Y. Ohgi, M. A. Minami, M. Jewariya, M. Nagai, T. Araki, and T. Yasui, "Real-time line projection for fast terahertz spectral computed tomography," Opt. Lett. **36**(11), 2119–2121 (2011).
10. M. Jewariya, E. Abraham, T. Kitaguchi, Y. Ohgi, M. A. Minami, T. Araki, and T. Yasui, "Fast three-dimensional terahertz computed tomography using real-time line projection of intense terahertz pulse," Opt. Express **21**(2), 2423–2433 (2013).
11. D. M. Mittleman, S. Hunsche, L. Boivin, and M. C. Nuss, "T-ray tomography," Opt. Lett. **22**(12), 904–906 (1997).
12. T. Yasuda, T. Yasui, T. Araki, and E. Abraham, "Real-time two-dimensional terahertz tomography of moving objects," Opt. Commun. **267**(1), 128–136 (2006).

#231148 - $15.00 USD Received 23 Dec 2014; revised 9 Feb 2015; accepted 9 Feb 2015; published 18 Feb 2015

13. J. Takayanagi, H. Jinno, S. Ichino, K. Suizu, M. Yamashita, T. Ouchi, S. Kasai, H. Ohtake, H. Uchida, N. Nishizawa, and K. Kawase, "High-resolution time-of-flight terahertz tomography using a femtosecond fiber laser," Opt. Express **17**(9), 7549–7555 (2009).
14. K. H. Jin, Y.-G. Kim, S. H. Cho, J. C. Ye, and D.-S. Yee, "High-speed terahertz reflection three-dimensional imaging for nondestructive evaluation," Opt. Express **20**(23), 25432–25440 (2012).
15. Y. Kim and D.-S. Yee, "High-speed terahertz time-domain spectroscopy based on electronically controlled optical sampling," Opt. Lett. **35**(22), 3715–3717 (2010).
16. S. Katletz, M. Pfleger, H. Pühringer, N. Vieweg, B. Scherger, B. Heinen, M. Koch, and K. Wiesauer, "Efficient terahertz en-face imaging," Opt. Express **19**(23), 23042–23053 (2011).
17. R. J. B. Dietz, N. Vieweg, T. Puppe, A. Zach, B. Globisch, T. Göbel, P. Leisching, and M. Schell, "All fiber-coupled THz-TDS system with kHz measurement rate based on electronically controlled optical sampling," Opt. Lett. **39**(22), 6482–6485 (2014).
18. Zemax demo can be downloaded at *http://www.zemax.com/support/downloads/download-demo*.
19. B. E. A. Saleh and M. C. Teich, *Fundamentals of Photonics* (Wiley-Interscience, 1991).

## 1. Introduction

Terahertz (THz) tomography can be used for nondestructive testing, due to the transparency of nonconductive materials to THz radiation [1–3]. Transmission-mode THz tomography requires the acquisition of projection images at various angles and image reconstruction [4–10]. For real-time B-scan (one-dimensional transverse scan along with axial scan) imaging or fast three-dimensional (3D) imaging, reflection-mode THz tomography utilizing time-of-flight information is more favorable than transmission-mode tomography because the former needs neither rotation for projection angles nor image reconstruction [11–13]. Recently, we demonstrated high-speed THz reflection 3D imaging by combining electronically-controlled optical sampling (ECOPS) with fast transverse moving of an imaging target using translation stages [14]. While A-scan (axial scan) data were acquired at 1 kHz scan rate using ECOPS measurement of THz time-domain waveforms [15], the total scan time for obtaining a 3D tomographic image was limited by the speed and acceleration of the translation stages.

In this work, we employ THz beam steering for a C scan (two-dimensional (2D) transverse scan) in order to overcome the limitation of total scan time due to translation stages. Beam steering can be implemented using a 2D galvanometer scanner with the help of a scanning lens. It was previously reported that a THz telecentric f-θ lens with axial symmetry was developed for beam steering in en-face imaging [16]. Here, we have developed a non-axially symmetric lens with superior characteristics as well as an axially symmetric lens. The characteristics of the lenses are demonstrated in the high-speed THz reflection 3D imaging system using beam steering. THz 3D tomographic images of a glass fiber reinforced polymer (GFRP) sample with artificial defects are also shown, acquired quickly using the imaging system.

## 2. High-speed THz reflection 3D imaging system using beam steering

Our imaging system is illustrated in Fig. 1. A vertically polarized THz pulse beam generated from a photoconductive antenna (PCA) THz emitter is collimated by an off-axis parabolic mirror. The collimated beam passes through a silicon beam splitter and is then steered with an optical angle (θ) of −20 ~ + 20 degree along both the X and Y directions by a 2D galvanometer scanner with a 25 mm aperture and a small-angle step response time of about 350 μs. Here, the optical angle refers to the angle between the optical axis and the direction of the beam. Regardless of the optical angle, the steered beam is perpendicularly incident on the focal plane through a THz telecentric f-θ lens. Also, the position of the focal point on the focal plane is equal to the product of the focal length of the lens and the optical angle in both the X and Y directions. The reflected beam from an imaging target placed on the focal plane goes back to the beam splitter along its initial path and is subsequently reflected from the beam splitter to be guided to a PCA THz detector by an off-axis parabolic mirror. THz time-domain waveforms are measured using ECOPS for time delay scanning, which are used as A-scan data. The detailed description of our ECOPS system can be found in [15]. In the ECOPS measurement, a time delay window of 52 ps is obtained with the scan rate set to 1 kHz, where the time delay varies linearly along with the real time. The time delay window of 52 ps

#231148 - $15.00 USD Received 23 Dec 2014; revised 9 Feb 2015; accepted 9 Feb 2015; published 18 Feb 2015

corresponds to an A-scan range of 7.8 mm in free space. A digital delay/pulse generator makes a 1 kHz TTL signal using a cross-correlation signal produced by a cross correlator [14]. Each A-scan data with 725 samples is acquired in approximately 240 μs at a scan rate of 1 kHz by a digitizer with a sampling rate of 3 MS/s triggered by the TTL signal. At the same time, the galvanometer scanner is driven by a waveform generator triggered by the TTL signal and the rotation angles of the galvanometer scanner are recorded to ensure that it is driven as planned.

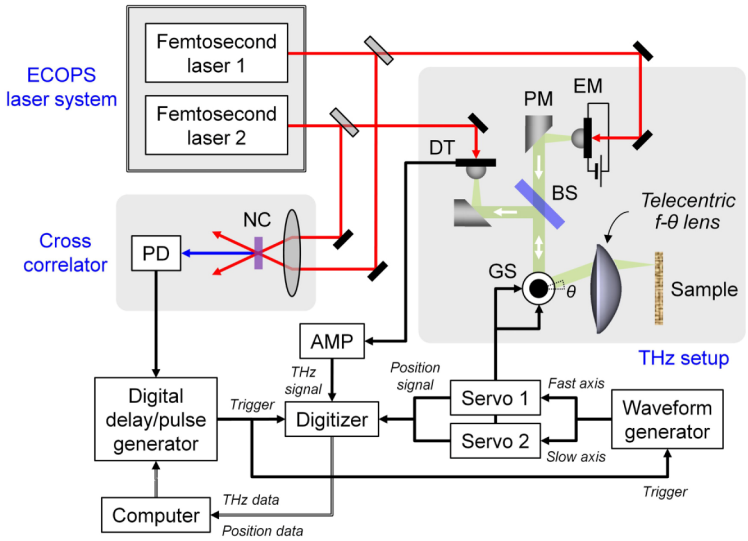


Fig. 1. Schematic diagram for our high-speed THz reflection 3D imaging system using beam steering. EM: THz emitter, PM: off-axis parabolic mirror, BS: silicon beam splitter, GS: 2D galvanometer scanner, DT: THz detector, AMP: current amplifier, NC: nonlinear crystal, PD: photodetector.

For a C-scan, we use the THz beam scanner that consists of a galvanometer scanner and lens. We acquire A-scan data while performing a raster scan with the beam scanner. A-scan data for 200 × 200 points in a C-scan range can be acquired in 40 s with an A-scan rate of 1 kHz. The total scan time can be reduced by decreasing the number of points. For instance, A-scan data for 100 × 100 points can be acquired in 10 s. Moving an imaging target for a C-scan with an A-scan rate of 1 kHz resulted in the total scan time being limited by the C-scan speed, i.e. the speed of translation stages [14]. With beam steering, on the contrary, the total scan time is limited by the A-scan rate of 1 kHz as the C-scan using beam steering is sufficiently fast. The total scan time could be shortened with a higher A-scan rate [17]. In beam steering, the total scan time does not depend on the C-scan range because the C-scan range is determined by the focal length of a telecentric f-θ lens and the optical angle range of a galvanometer scanner, unlike with when moving an imaging target. Also, in this situation, we do not have to use triangle-based linear interpolation to regrid raw data into a regular 3D data cube since the positions where the A-scan data are acquired are regular due to a raster scan, whereas interpolation had to be conducted when moving an imaging target along a zigzag trajectory [14].

### 3. Design and manufacture of THz telecentric f-θ lenses

We have constructed a THz beam scanner consisting of a galvanometer scanner and a scanning lens in order to implement beam steering in the imaging system as described above. Figure 2(a) simply illustrates the operation of a beam scanner. The scanning lens was designed to have telecentricity and an f-θ characteristic [16]. Since a beam steered by a galvanometer scanner is perpendicularly incident on a focal plane through a telecentric lens irrespective of the optical angle, a telecentric lens allows the reflected beam from an imaging target placed on the focal plane to return to the beam splitter along its original path. Also, due

#231148 - $15.00 USD Received 23 Dec 2014; revised 9 Feb 2015; accepted 9 Feb 2015; published 18 Feb 2015

to the f-θ characteristic, the position of the focal point on the focal plane is equal to the product of the focal length of the lens and the optical angle in both the X and Y directions. C-scan images can be displayed with respect to optical angles without image distortion because the position of the focal point is linearly proportional to the optical angle.

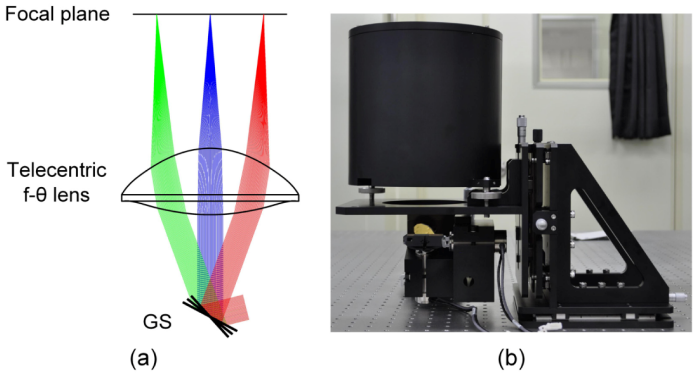


Fig. 2. (a) Simple illustration showing the operation of the beam scanner. (b) Picture of the developed beam scanner.

To meet the requirements of the scanning lens while minimizing attenuation of the THz beam by the scanning lens, a single aspheric lens was chosen instead of multiple lenses. First, an axially symmetric lens was designed with an even aspheric surface type [16]. Since the X and Y galvanometer mirrors, which should be located at the back focal point of the scanning lens for complete telecentricity, actually stand apart, we predicted that a non-axially symmetric lens, which has bilateral symmetry on both the X and Y axes, would have better characteristics than an axially symmetric lens. Thus, a non-axially symmetric lens was designed with an anamorphic aspheric surface type [18].

Polytetrafluoroethylene (PTFE), one of the materials with the lowest reflection and absorption losses in the THz region, was chosen as the lens material. An optical design software (Zemax) was used to design scanning lenses that have telecentricity, an f-θ characteristic, and a C-scan range of 100 × 100 $mm^2$. Through a sequential ray-tracing simulation of an optical system consisting of a galvanometer scanner, a scanning lens, and a focal plane, the shape of the scanning lens was optimized to minimize the merit function including the incidence angle of the chief ray on the focal plane, the deviation from the f-θ condition, and the beam spot size on the focal plane.

In accordance with the lens designs, we manufactured an axially symmetric lens and a non-axially symmetric lens by machining the PTFE. To align the galvanometer scanner and scanning lens with the THz beam, we also designed and fabricated lens holders, lens mounts for tilt adjustment, and translation stages for the galvanometer scanner and the scanning lens, as shown in Fig. 2(b).

## 4. Performance evaluation of THz telecentric f-θ lenses

To evaluate the performances of the lenses, we prepared a flat metal mirror and a pattern mask with a chrome grid pattern on a soda-lime glass plate. Figure 3(a) shows the optimized design of the axially symmetric lens. The C-scan image of the pattern mask acquired using the axially symmetric lens is shown in Fig. 3(b), constructed from the maximum amplitudes of the A-scan data. The C-scan data were normalized using that of the flat metal mirror. The image appears close to the grid pattern with respect to the optical angles but has a slight distortion. That is, the axially symmetric lens shows a small deviation from the f-θ condition. The optical path length difference (OPLD) image of the flat metal mirror is displayed in Fig. 3(c), constructed from the axial positions of the THz pulses in the A-scan data. Figures 3(d) and 3(e) show the B-scan images of the flat metal mirror on the X and Y axes, respectively, where the axial position of the THz pulse varies with the optical angle. The maximum one-way OPLD throughout the C-scan area is 1.77 mm, as shown in Fig. 3(c).

#231148 - $15.00 USD Received 23 Dec 2014; revised 9 Feb 2015; accepted 9 Feb 2015; published 18 Feb 2015

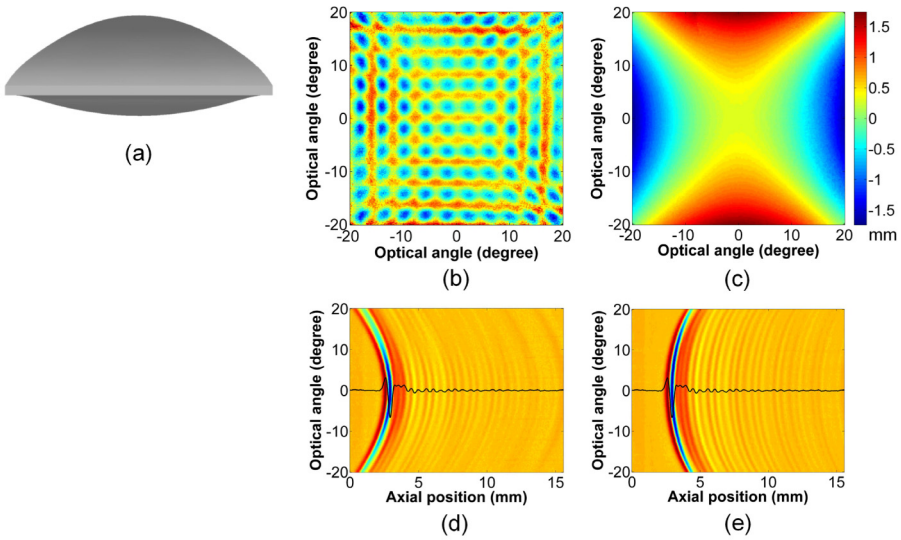


Fig. 3. (a) Design for the axially symmetric lens. C-scan image (b) of the grid-pattern mask, OPLD image (c) of the flat metal mirror, and B-scan images ((d) and (e)) of the flat metal mirror on the X and Y axes, respectively, obtained using the axially symmetric lens.

Figure 4(a) displays the optimized design of the non-axially symmetric lens. The C-scan image of the pattern mask acquired using the non-axially symmetric lens is indicated in Fig. 4(b). The image appears closer to the grid pattern than the image shown in Fig. 3(b) with respect to the optical angles. This indicates that the non-axially symmetric lens has a superior f-θ characteristic. The OPLD image of the flat metal mirror is also displayed in Fig. 4(c). Figures 4(d) and 4(e) represent the B-scan images of the flat metal mirror on the X and Y axes, respectively, where the change in the axial position of the THz pulse with the optical angle is much smaller than in Figs. 3(d) and 3(e). The maximum one-way OPLD is as small as 0.42 mm, as shown in Fig. 4(c). From the OPLD results in Figs. 3(c) and 4(c), it is apparent that the non-axially symmetric lens is superior to the axially symmetric lens in telecentricity [16]. A smaller OPLD allows us to secure a longer available A-scan range within the limited A-scan range determined by the ECOPS system. Compensation of an acquired 3D image for the OPLD can be performed using the OPLD image.

To estimate the transverse resolution of the imaging system, we obtained the C-scan image of the flat metal mirror that covers half of the C-scan area. The C-scan image acquired using the non-axially symmetric lens is shown in Fig. 5, where the mirror lies at the red area. The black line represents the C-scan data along the Y axis, whose derivative is indicated by the yellow line. The full width at half maximum (FWHM) of the yellow line is around 4 mm, which is comparable to the FWHM measured along the X axis. Thus, the transverse resolution can be estimated as approximately 4 mm. For the axially symmetric lens, the transverse resolution is almost identical to that of the non-axially symmetric lens. The transverse resolution depends on the beam spot size on the focal plane. The THz pulse measured in the imaging system has a broadband amplitude spectrum in which the frequency band has a mean frequency of about 0.4 THz when weighted with the amplitude. Assuming the THz beam as a Gaussian beam, the beam spot size is estimated as 5.5 mm by $(4/\pi)(f\lambda/D)$ where $f$ is the focal length of the lenses, $\lambda$ is the wavelength corresponding to the mean frequency, and $D$ is the input beam diameter [19]. The FWHM of the beam spot is also estimated as 4.5 mm by $\sqrt{\ln 2}\,(4/\pi)(f\lambda/D)$, which is similar to the measured FWHM when it is considered that the point-to-point interval is about 0.5 mm in the C scan. Hence, the aberration effect of the lenses on the beam spot size and the transverse resolution can be

#231148 - $15.00 USD Received 23 Dec 2014; revised 9 Feb 2015; accepted 9 Feb 2015; published 18 Feb 2015

regarded as negligible. Due to the f-θ characteristic of the lenses, the C-scan range is determined by the focal length of the lenses with the optical angle range fixed. Thus, the C-scan range can be increased by using a telecentric f-θ lens with a longer focal length. However, a longer focal length also increases the beam spot size, thereby reducing the transverse resolution.

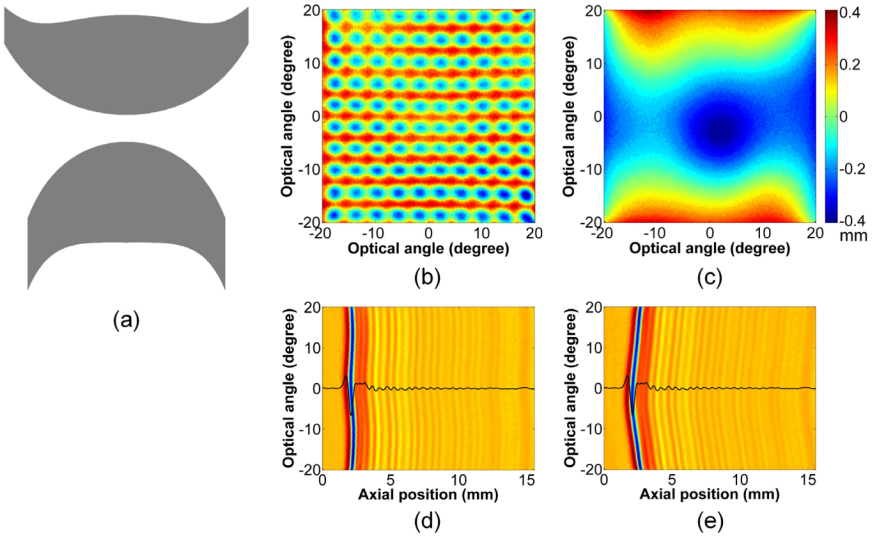


Fig. 4. (a) Design for the non-axially symmetric lens. The upper and lower figures indicate the cross-sectional views in the X and Y directions, respectively (See Media 1 for the 3D design). C-scan image (b) of the grid pattern mask, OPLD image (c) of the flat metal mirror, and B-scan images ((d) and (e)) of the flat metal mirror on the X and Y axes, respectively, obtained using the non-axially symmetric lens.

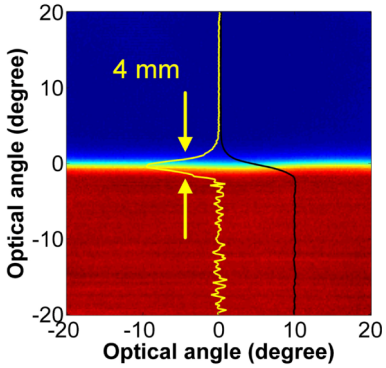


Fig. 5. C-scan image of the flat metal mirror covering half of the C-scan area. The black line shows the C-scan data along the Y axis, whose derivative is indicated by the yellow line.

## 5. 3D imaging of a GFRP sample with artificial internal defects

Using the imaging system that can completely scan a volume of 100 × 100 × 7.8 $mm^3$ in 40 s, yielding 200 × 200 × 725 voxels, we acquired images of a GFRP sample with artificial internal defects. By using translation stages to move the sample, we previously obtained the THz 3D image of the sample whose schematic design is displayed in Fig. 6(a) [14]. The sample dimensions are 100 mm, 100 mm, and 3 mm in width, length, and thickness, respectively. Delaminations with a nominal thickness of 0.2 mm lie at depths of 1 mm and 2 mm and pieces of PTFE with a nominal thickness of 0.025 mm are included at a depth of 1.5

#231148 - $15.00 USD Received 23 Dec 2014; revised 9 Feb 2015; accepted 9 Feb 2015; published 18 Feb 2015

mm, as illustrated in Fig. 6(a). Figures 6(b) and 6(c) depict the C-scan images of the sample acquired using the axially and non-axially symmetric lenses, respectively. They were constructed from the maximum amplitudes of the A-scan data, with the data from the front and back surfaces excluded. The images of the lower delaminations are less clear than those of the upper ones due to attenuation of THz waves by the GFRP. The images of the defects are affected by the incomplete telecentricity of the lenses as well. Since the axially symmetric lens causes a greater increase in the incidence angle with the optical angle than the non-axially symmetric lens, the signal-to-noise ratio around the edge is higher with the non-axially symmetric lens. Thus, the lower delaminations are more clearly visualized with the non-axially symmetric lens than with the axially symmetric lens. The PTFE inclusions are barely visible owing to their thinness [14].

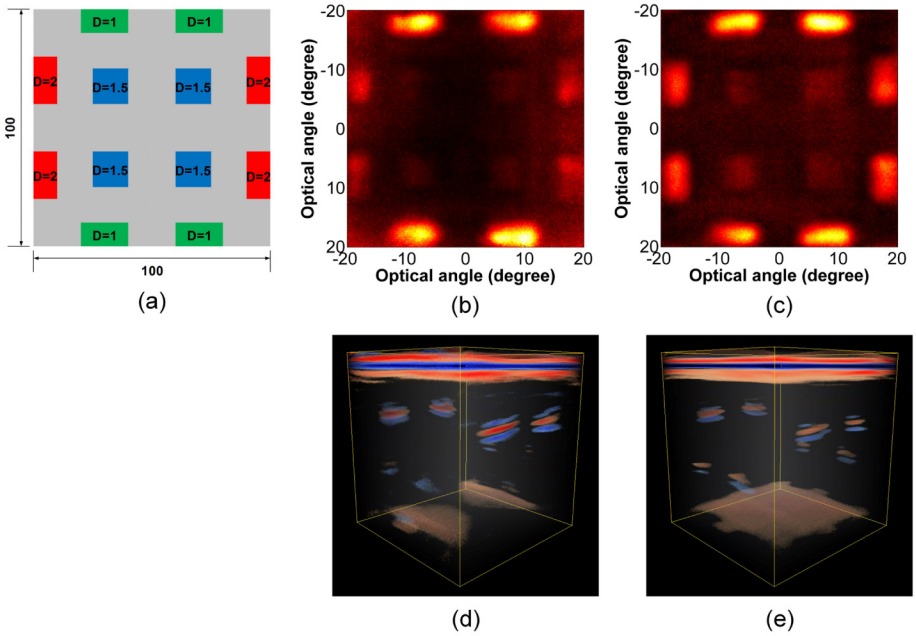


Fig. 6. (a) Schematic design for the GFRP sample. The blue squares represent PTFE inclusions and the green and red rectangles represent delaminations. The depths at which the defects lie are indicated in the design. The numbers are presented in millimeters. (b) and (c) C-scan images of the GFRP sample obtained using the axially and non-axially symmetric lenses, respectively. (d) and (e) 3D tomographic images of the GFRP sample obtained using the axially and non-axially symmetric lenses, respectively (Media 2 and Media 3).

We also made 3D data cubes by compensating the raw data for the OPLDs using the OPLD images from the flat mirror. The 3D volume of the sample was rendered using a rendering method that depicts the values around a noise level as transparent and the values around the maximum and minimum as opaque colors. The 3D tomographic images of the sample obtained using the axially and non-axially symmetric lenses are shown in Figs. 6(d) and 6(e), respectively. The lower delaminations are more clearly visible with the non-axially symmetric lens than with the axially symmetric lens, similar to the C-scan images. Due to the limited A-scan range and the larger OPLD of the axially symmetric lens, the back surface is partially visible in Fig. 6(d). In contrast, the smaller OPLD of the non-axially symmetric lens enables full visualization of the back surface as shown in Fig. 6(e).

## 6. Conclusion

We have demonstrated high-speed THz reflection 3D imaging using ECOPS measurement and beam steering. The ECOPS measurement of THz waveforms enables acquisition of A-scan data with a scan range of 7.8 mm at a scan rate of 1 kHz. A-scan data for 200 × 200

#231148 - $15.00 USD Received 23 Dec 2014; revised 9 Feb 2015; accepted 9 Feb 2015; published 18 Feb 2015

points in a C-scan range of 100 × 100 $mm^2$ can be acquired in 40 s while performing a fast C-scan by virtue of beam steering. The total scan time can be reduced by decreasing the number of points. For beam steering, we developed THz telecentric f-θ lenses with axial and non-axial symmetry, and it was experimentally demonstrated that the non-axially symmetric lens had better performance than the axially symmetric lens. Using the imaging system, a GFRP sample with defects, which had a volume of 100 × 100 × 3 $mm^3$, was fully scanned in 40 s and its THz 3D tomographic image with 200 × 200 × 725 voxels was successfully acquired. Consequently, the restriction to total scan time by the speed of the translation stages when moving an imaging target was overcome by using beam steering.

The THz setup including the beam scanner in Fig. 1 could be advanced to a portable scanning head by employing a fiber-coupled THz emitter and detector. Furthermore, this fast 3D imaging technology using beam steering could open the door to fast portable THz 3D imaging instruments based on a portable scanning head and an ECOPS fiber-laser system, which have the potential for practical applications without the need to move an imaging target.

**Acknowledgment**

This work was supported in part by the National Research Foundation of Korea - Grant funded by the Korean Government (NRF-2012-M2A2A9-2012035659) and in part by the Ministry of Science, ICT, and Future Planning through the project KRISS-14011055.

#231148 - $15.00 USD Received 23 Dec 2014; revised 9 Feb 2015; accepted 9 Feb 2015; published 18 Feb 2015